Long-Wavelength AIE-based Fluorescent Probes for Mitochondria-Targeted Imaging and Photodynamic Therapy of Hepatoma cells

Dan Zhao,[a‡] Hai-Hao Han,[a‡] Ling Zhu,[a] Fang-Zhou Xu,[a] Xing-Yu Ma,[a] Jia Li,[b] Tony D. James,[c,d]* Yi Zang,[b]* Xiao-Peng He,[a]* and Chengyun Wang[a]*

[a] *Key Laboratory for Advanced Materials and Joint International Research Laboratory of Precision Chemistry and Molecular Engineering, Feringa Nobel Prize Scientist Joint Research Center, Frontiers Center for Materiobiology and Dynamic Chemistry, School of Chemistry and Molecular Engineering, East China University of Science and Technology, 130 Meilong Rd., Shanghai 200237, China.*

[b] *National Center for Drug Screening, State Key Laboratory of Drug Research, Shanghai Institute of Materia Medica, Chinese Academy of Sciences, 189 Guo Shoujing Rd., Shanghai 201203, P. R. China.*

[c] *Department of Chemistry, University of Bath, Bath, BA2 7AY, UK.*

[d] *School of Chemistry and Chemical Engineering, Henan Normal University, Xinxiang 453007, China.*

ABSTRACT: With this research, we have developed two long-wavelength theranostic probes (**DCMT** and **DCMC**) with aggregation-induced emission (AIE)-based properties for image-guided photodynamic therapy (PDT) of hepatoma cells. Introduction of a triphenylamine or carbazole group to a dicyanomethylene-4*H*-pyran dye with long-wavelength fluorescence emission produces the AIE-based probes, which were subsequently modified with triphenyl-phosphonium cation for actively targeting the mitochondria of hepatoma cells. Solution-based experiments show that the probes exhibit a mixed photophysical mechanism of twisted-intramolecular charge transfer and AIE at different aggregation states. The molecular aggregation of the probes also leads to an enhanced ability for oxygen photosensitization, suggesting their potential for PDT of cancer cells. Our subsequent cell-based assays show that the probes localize in the mitochondria of hepatoma cells, and the use of light leads to cell death through the intracellular production of reactive oxygen species.

KEYWORDS: Aggregation-induced emission (AIE), Photodynamic therapy (PDT), Photosensitizer, Mitochondria, Theranostic probe

INTRODUCTION

The progression of cancer is usually associated with the functional impairment of mitochondrion including an increase in reactive oxygen species (ROS) levels and metabolic disorders of the mitochondria.[1,2] Mitochondria are considered to be the powerhouse of cells, and are also where most intracellular ROS is produced, modulating signaling relevant to cell death. The mitochondrial membrane potential of cancer cells is more negative than that of normal cells, which allows mitochondria-targeted chemical tools to selectively accumulate in cancer cells.[3] Therefore, targeting the mitochondria of cancer cells has become a promising strategy for targeted cancer therapy.[4] Compared with conventional radio- and chemotherapy, photodynamic therapy (PDT) is an emergent technology for cancer treatment with advantages in terms of side effects, invasiveness and drug resistance.[5,6] The mechanism of PDT is that a photosensitizer (PS) reacts with O_2 under light irradiation to produce reactive oxygen species (ROS) (e.g. in the form of singlet oxygen ($^1O_2$)), leading to damage of cellular components.[7,8] As a result, the ability to accurately localize PDT agents to cancer cells is key to the efficacy of PDT-based therapy.

Image-guided cancer therapy has become a topical research area in biomedicine. To achieve this goal, a fluorescent probe is covalently conjugated with a drug molecule, producing an activatable prodrug system that responds to specific biospecies in a cancer microenvironment for image-guided therapy. Many elegant theranostic probes have been developed over the past decade.[9-24] However, most of the probes developed to date have been based on aromatic dyes that tend to aggregate in aqueous media, leading to aggregation-caused quenching (ACQ), which lowers the imaging capacity of the systems. In addition, the majority of the theranostic probes developed are based on the release of cytotoxic drugs in cancer cells, which could be accompanied by drug-resistance issues.

Aggregation-induced emission (AIE) is a photophysical phenomenon first coined by Tang's group in 2001.[25,26] Restriction of intramolecular rotation (RIR) has been the most recognized AIE mechanism.[27] In addition to their usefulness in long-term fluorescence-based bioimaging,[28,29] AIE-based compounds have also been reported to serve as robust PSs. It is reported that traditional ACQ-based PSs undergo nonradioactive decay as a result of π−π stacking, leading to a quenched lowest singlet state (S1), and thus a low $^1O_2$ yield.[30] In contrast, AIE-based dyes overcome this issue through aggregation-induced excitonic orbital overlap leading to energy splitting, which enhances the intersystem crossing (ISC) efficiency.[31] With this research we have developed two AIE-based theranostic probes, **DCMT** and **DCMC**, for the mitochondria-targeted, image-guided PDT of liver cancer cells (Hep-G2) (Scheme 1).

EXPERIMANTAL

Instruments and Materials. All chemicals used in the synthesis were purchased from Taitan and used without further purification. All solvents are purified and dried according to standard procedures. The ^{1}H NMR spectra were recorded on a Bruker AV-400 NMR spectrometer using $CDCl_3$ or DMSO-d_6 as solvent. ^{13}C NMR spectra were recorded on an Ascend 600 NMR spectrometer with DMSO-d_6 as solvent. The mass spectra were obtained using a Waters LCT Premier XE mass spectrometer. A Varian Cary 60 was used to measure the UV-vis spectra, and Varian Cary Eclipse was used to obtain fluorescence spectra. A GeminiSEM 500 was used to obtain morphology images. DLS was obtained using a Nicomp 380 ZLS. A FLS-980 was used to get fluorescence quantum yields. An Electro-Spin Resonance Spectrometer was used to collect electron paramagnetic resonance (EPR) spectra. All the cells used for the co-localization and PDT experiments were HepG2 cells, which were obtained from ATCC (American Type Culture Collection).

Scheme 1. Synthesis of the AIE-based theranostic probes DCMT and DCMC

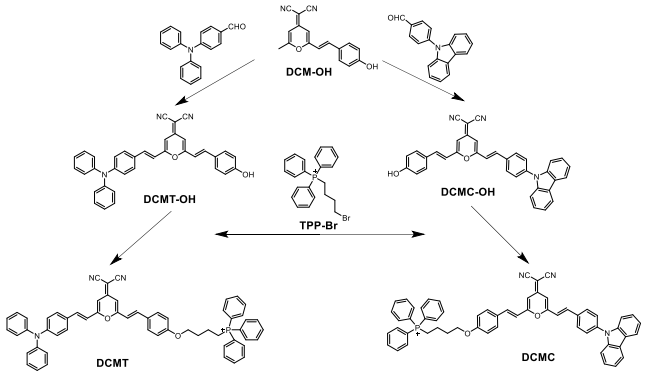

Synthesis of DCMT and DCMC. Compound DCM-OH and triphenyl phosphobromine salt (TPP-Br) were prepared according to the reported procedures [32,33]

Synthesis and characterization of DCMT-OH. DCM-OH (342 mg, 1.24 mmol) and 4-(diphenylamino) benzaldehyde (372 mg, 1.36 mmol) were dissolved in 20 mL acetonitrile, then piperidine (0.5mL) was added and the mixture was heated at reflux overnight. The reaction mixture was cooled to room temperature and the solvent was removed under vacuum, and the residue was purified using silica chromatography (dichloromethane as eluent) to obtain DCMT-OH as a dark red solid (296 mg, yield 45%). ^{1}H NMR (400 MHz, DMSO-d_6) δ (ppm): 10.09 (s, 1H, -OH), 7.73 – 7.63 (m, 6H, Ar-H), 7.38 (t, *J* = 7.9 Hz, 4H, Ar-H), 7.20 – 7.09 (m, 8H, Ar-H), 6.94 (d, *J* = 8.4 Hz, 2H, -CH=CH-), 6.84 (d, *J* = 8.3 Hz, 2H, -CH=CH-), 6.79 (d, *J* = 4.5 Hz, 2H, -CH=C-). ^{13}C NMR (150 MHz, DMSO-d_6) δ 191.42, 163.78, 160.20, 159.92, 159.70, 156.48, 149.56, 146.79, 138.49, 137.74, 132.57, 130.65, 130.26, 130.04, 130.01, 128.89, 128.60, 126.67, 125.70, 124.78, 121.33, 117.04, 116.43, 116.33, 116.30, 116.11, 106.74, 106.40. HRMS: Calcd for $C_{36}H_{24}N_3O_2$ ([M-H]$^-$), 530.1869; found: 530.1866.

Synthesis and characterization of DCMC-OH. To a solution of DCM-OH (300 mg, 1.09 mmol) and 4-(diphenylamino) benzaldehyde (324 mg, 1.20 mmol) in 20 mL acetonitrile, piperidine (0.5 mL) was added and the mixture was heated at reflux overnight. After the reaction mixture cooled, the solvent was removed under reduced pressure, and the residue purified by silica chromatography (dichloromethane as eluent) to give DCMC-OH as a dark red solid (309 mg, yield 54%). ^{1}H NMR (400 MHz, DMSO-d_6) δ (ppm): 9.79 (s, 1H,-OH), 8.28 (d, 2H, *J* = 7.2 Hz, Ar-H), 8.11 (d, 2H, *J* = 7.4 Hz, Ar-H), 7.91 (d, *J* = 16.2 Hz, 1H, -CH=C-), 7.73 (m, 4H, Ar-H), 7.70 (d, 2H, *J* = 7.9 Hz, Ar-H), 7.50 (m, 4H, Ar-H), 7.33 (d, 2H, *J* = 8.3 Hz, Ar-H), 7.21 (d, *J* = 16.4 Hz, 1H, -CH=C-), 6.94 (d, *J* = 7.0 Hz, 2H, -CH=CH-), 6.87 (d, *J* = 9.0 Hz, 2H, -CH=CH-). ^{13}C NMR (150 MHz, DMSO-d_6) δ 191.43, 163.81, 163.78, 160.29, 160.14, 159.05, 156.59, 140.26, 138.62, 136.88, 134.58, 132.58, 130.74, 130.27, 128.90, 127.27, 126.86, 126.69, 123.46, 121.07, 120.86, 116.39, 116.31, 116.04, 110.30, 107.90, 106.60. HRMS: Calcd for $C_{36}H_{22}N_3O_2$ ([M-H]$^-$), 528.1712; found: 528.1726.

Synthesis and characterization of DCMT. A solution of DCMT-OH (150 mg,0.28mmol), TPP-Br (202 mg, 0.42 mmol), KI (23 mg, 0.14 mmol) and K_2CO_3 (78 mg, 0.56 mmol) in anhydrous N, N-dimethylformamide (DMF, 10 mL) was heated to 130°C and stirred overnight. The mixture was then poured into deionized water (75 mL) and a black solid precipitated. The solid was purified using column chromatography (DCM: MeOH=50:1), resulting in DCMT as a dark red solid (168 mg, yield 65%). ^{1}H NMR (400 MHz, DMSO-d_6) δ (ppm): 7.92 (d, *J* = 8.2 Hz, 2H, Ar-H), 7.86 (d, *J* = 19.8 Hz, 2H, Ar-H), 7.83-7.71 (m, 15H, Ar-H), 7.69 (d, *J* = 8.9 Hz, 2H, Ar-H), 7.38 (t, *J* = 16.0 Hz, 4H, Ar-H), 7.26 (d, *J* = 13.1 Hz, 1H, Ar-H), 7.22 (d, *J* = 12.9 Hz, 1H, Ar-H), 7.17 (d, *J* = 7.4 Hz, 2H, Ar-H), 7.12 (d, *J* = 7.7 Hz, 4H, Ar-H), 6.98 (d, *J* = 8.6 Hz, 2H, -CH=CH-), 6.95 (d, *J* = 8.6 Hz, 2H, -CH=CH-), 6.82 (s, 2H, -CH=C-), 4.12 (t, *J* = 11.2 Hz, 2H, -CH_2-), 3.68 (t, *J* = 15.0 Hz, 2H, -CH_2-), 1.94 (t, *J* = 12.4 Hz, 2H, -CH_2-), 1.73 (t, *J* = 22.4 Hz, 2H, -CH_2-). ^{13}C NMR (150 MHz, DMSO-d_6) δ 160.56, 159.74, 159.63, 156.44, 149.54, 146.72, 137.83, 137.79, 135.36, 135.34, 134.11, 134.04, 133.97, 133.94, 133.84, 130.78, 130.71, 130.63, 130.57, 130.52, 130.32, 130.22, 130.14, 130.01, 129.98, 129.86, 128.54, 128.19, 125.65, 125.38, 124.75, 124.67, 121.26, 119.17, 118.60, 117.21, 116.98, 116.21, 116.18, 115.37, 115.33, 106.74, 66.62, 55.97, 29.38, 26.74. HRMS: Calcd for $C_{58}H_{47}N_3O_2P$ ([M]$^+$), 848.3406; found: 848.3404.

Synthesis and characterization of DCMC. A solution of DCMC-OH (150 mg, 0.28 mmol), TPP-Br (200 mg, 0.42 mmol), KI (23 mg, 0.14 mmol) and K_2CO_3 (78 mg, 0.56 mmol) in anhydrous N, N-dimethylformamide (DMF, 10 mL) was heated to 60°C and stirred for two hours. The mixture was then poured into deionized water (75 mL) and a black solid precipitated. The product was purified using column chromatography (DCM: MeOH = 50: 1), producing DCMC as brown solid (130 mg, yield 50%). ^{1}H NMR (400 MHz, DMSO-d_6) δ (ppm): δ 8.28 (d, *J* = 7.7 Hz, 2H, Ar-H), 8.12 (d, *J* = 8.4 Hz, 2H, Ar-H), 7.95- 7.90 (m, 4H, Ar-H), 7.84 (s, 2H, -CH=C-), 7.83-7.70 (m, 15H, Ar-H), 7.57 (d, *J* = 16.2 Hz, 1H, Ar-H), 7.51-7.45 (m, 4H, Ar-H), 7.35-7.29 (m, 3H, Ar-H), 7.01 (d, *J* = 8.7 Hz, 2H, -CH=CH-), 6.97 (d, 1H, *J* = 2.0 Hz, -CH=CH-), 6.88 (d, *J* = 2.0 Hz, 1H, -CH=CH-), 4.12 (t, *J* = 5.9 Hz, 2H, -CH_2-), 3.68 (t, *J* = 8.8 Hz, 2H, -CH_2-), 1.94 (t, *J* = 13.2 Hz, 2H, -CH_2-), 1.73 (t, *J* = 22.0 Hz, 2H, -CH_2-). ^{13}C NMR (150 MHz, DMSO-d_6) δ 160.63, 159.81, 159.05, 156.52, 140.18, 138.59, 138.17, 136.90, 135.40, 135.36, 135.34, 134.51, 134.05, 133.98, 130.81, 130.79, 130.74, 130.71, 130.63, 130.39, 130.23, 130.19, 128.20, 127.20, 126.80, 126.76, 123.40, 121.03, 120.81, 119.17, 118.60, 118.55, 117.14, 116.02, 115.40,

110.22, 107.90, 106.93, 66.64, 56.92, 29.45, 26.65. HRMS: Calcd for $C_{58}H_{45}N_3O_2P$ ([M]$^+$), 846.3249; found: 846.3235.

RESULTS AND DISCUSSION

Design and Synthesis of DCMT and DCMC. Triphenylamine (TPA) and carbazole (CBZ) are commonly used functional groups to enhance the AIE effect of fluorescent dyes.[2] A simple Knoevenagel condensation reaction was used to connect TPA and CBZ to an orange-red-emitting DCM (dicyanomethylene-4*H*-pyran) dye,[34] producing **DCMT-OH** and **DCMC-OH** with AIE-based properties, respectively. To target mitochondria, both **DCMT-OH** and **DCMC-OH** were equipped with a triphenyl-phosphonium cation,[35,36] producing the **DCMT** and **DCMC**, respectively. A recent study indicated that when an appropriate D-A (donor-acceptor) structure is introduced to an AIE-based PSs, the ROS generation efficiency was enhanced.[37] Compared to **DCMC**, the TPA group in **DCMT** is conformationally less rigidified, which might lead to a difference in photophysical and biological properties.[38]

Optical properties of DCMT and DCMC. With these compounds in hand, we evaluated their photophysical properties. **DCMT** exhibited an absorption maximum at 445 nm in water (Fig. S13A, ESI, blue), and a fluorescence emission maximum was observed at 663 nm (Fig. S13A, ESI, red) under 445 nm excitation. The absorption and emission maximum for **DCMC** was determined to be 425 nm (Fig. S13B, ESI, blue) and 650 nm (Fig. S13B, ESI, red), respectively. Both probes exhibit a large stokes shift (218 nm and 225 nm for **DCMT** and **DCMC**, respectively). In addition, we determined that solvent polarity had minimal effect on the absorption spectra of **DCMT** and **DCMC** (Fig. S14, ESI). However, with an increase of solvent polarity, their emission maximum red-shifted (Figure S14, ESI), characteristic of a TICT (twisted-intramolecular charge transfer) process in D-A structrures.[39] The fluorescence quantum yields of **DCMT** and **DCMC** in water were determined to be 1.05% and 5.59%, respectively, using a fluorescence spectrophotometer with an integrating sphere. The molar extinction coefficient of **DCMT** and **DCMC** was determined to be 12218 $cm^{-1}mol^{-1}$ L and 14686 $cm^{-1}mol^{-1}$ L, respectively (Table S1, ESI).

AIE properties of DCMT and DCMC. Next, the AIE properties of **DCMT** and **DCMC** in a solvent mixture of DMSO/water were evaluated. As shown in Figure 1A and 1B, we determined that the fluorescence intensity of **DCMT** gradually decreased with an increasing water to DMSO ratio from 0 to 0.5; the decreased fluorescence intensity is probably the result of a TICT effect for **DCMT** in polar solvents.[40,41] When the water fraction was further increased (up to 90%), the fluorescence intensity significantly increased, which could be ascribed to the RIR-based AIE effect due to aggregation of the **DCMT** molecules in a water system.[42] When the water fraction was increased from 90% to 99%, the fluorescence intensity decreased, which may be due to the spontaneous fluorescence absorption of numerous molecular aggregates and changes in the aggregate morphology.[40,41] The change in fluorescence intensity of **DCMC** with increasing water in DMSO was like that of **DCMT** (Fig. 1C and 1D). An additional viscosity experiment showed that an increase in viscosity led to a much shaper fluorescence enhancement of **DCMT** than **DCMC** (Figure S15, ESI).[43,44]

Scanning electron microscopy (SEM) and dynamic light scattering (DLS) were then used to examine the morphological changes of the probes in solutions with an increasing water fraction (Fig. S16, ESI). We observed that with a small fraction of water in DMSO (20%, v/v), both **DCMT** (Fig. S16A, ESI) and **DCMC** (Fig. S16D, ESI) appeared to be amorphous from their representative SEM images with an average hydrodynamic diameter of 206.1 nm and 155.2 nm, respectively. With an increase of water fraction, however, both compounds formed structurally defined particles. With a water fraction in DMSO of 50% (v/v), nanoparticles with a diameter of 77.8 nm and 74.4 nm were observed for **DCMT** (Fig. S16B, ESI) and **DCMC** (Fig. S16E, ESI), respectively. The particle size of **DCMT** (Fig. S16C, ESI) and **DCMC** (Fig. S16F, ESI) aggregates further decreased to 62.4 nm and 51.3 nm when the water fraction was increased to 90% (v/v) and 70% (v/v), respectively. These results suggest that (1) the probes are not orderly self-assembled in a good solvent, thus exhibiting TICT-caused fluorescence quenching,[45] and (2) in a poor solvent these amphiphiles self-assemble to form nanoparticles with an enhanced fluorescence, which agrees with previous reports on AIE-based nanoparticle systems.[46]

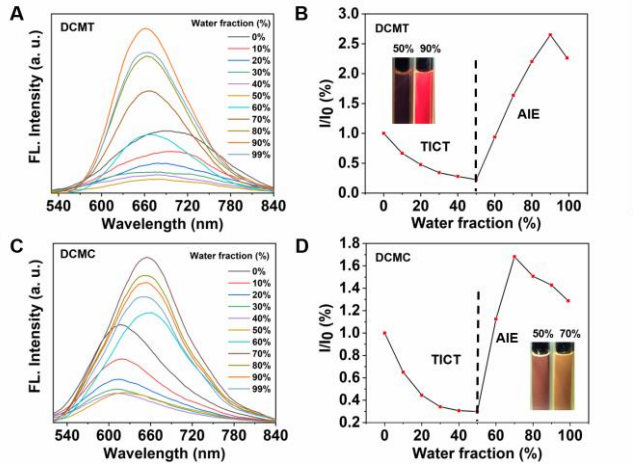

Figure 1. Fluorescence spectra of (A) **DCMT** and (C) **DCMC** (10 μM) in different DMSO/water mixtures. Plotting the fluorescence intensity change of (B) **DCMT** and (D) **DCMC** (10 μM) (where I and I_0 are the changed and initial fluorescence of the probe, respectively) as a function of water fraction in the DMSO/water mixtures.

The production of ROS and singlet oxygen. $^1O_2$ is the key cytotoxic agent leading to cells death in PDT. Thus, the ability of **DCMT** and **DCMC** to produce $^1O_2$ were evaluated using a commercial indicator, 9,10 anthracenediyl-bis(methylene)-dimalonic acid (ABDA) in water after broad-band irradiation (22.7 mW cm^{-2}). It can be seen from Fig. 2A (**DCMT**) and Fig. 2B (**DCMC**) that with irradiation time, the characteristic absorption peaks of ABDA decreased gradually. Using Rose Bengal (RB) as a reference ($^1O_2$ quantum yield = 0.75 in water) (Fig. 2C),[47-49] the $^1O_2$ quantum yield of **DCMT** and **DCMC** was determined to be 0.87 and 0.78, respectively. The $^1O_2$ quantum yields of **DCMT-OH**/**DCMC-OH** (0.45/0.32) were determined to be much lower (Fig. S18 and S19, ESI) than those of **DCMT** and **DCMC**, which might be caused by the exposure of the phenol group that inhibits the generation of free radicals. Figure 2D shows that both **DCMT** and **DCMC** produced $^1O_2$ more rapidly than the commercial RB, which is indicative of potential use in cellular experiments. Electron paramagnetic resonance (EPR) spectroscopy was used to further prove $^1O_2$ generation of **DCMT** and **DCMC** (Figure S23, ESI). It was

seen that the EPR signals of **DCMT** and **DCMC** with 2,2,6,6-tetramethylpiperidine (TEMP) was significantly enhanced after white light irradiation for 10 min, corroborating the $^1O_2$ production of the probes. The ΔE_{ST} (energy difference between S1 and T1 state) value of **DCMT** and **DCMC** was determined to be 0.5380 and 0.6131 eV, respectively, by density functional theory (Tables S2 and S3, ESI). The smaller ΔE_{ST} value of **DCMT** agrees with its higher $^1O_2$ conversion efficiency than **DCMC**.[50]

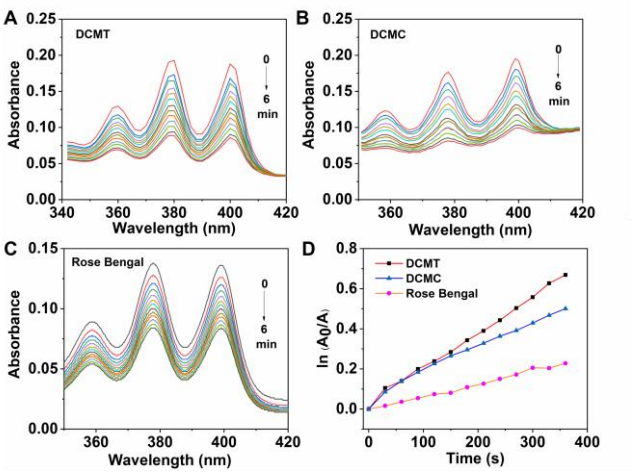

Figure 2. UV-vis absorption spectra of ABDA (50 μM) in the presence of (A) **DCMT** (5 μM), (B) **DCMC** (5 μM), and (C) Rose Bengal (5 μM) in water under white light irradiation (22.7 mW cm^{-2}) every 30 seconds for 6 min. (D) Plotting the absorption change of ABDA at 380 nm in **DCMT**, **DCMC** and RB water solution after white-light irradiation with time.

Cell Imaging of DCMT/DCMC in Mitochondria. Next, we turned our attention to the evaluation of the theranostic properties towards cancer cells. HepG2 (human hepatoma) was used as a model cancer cell line. Confocal laser-scanning microscopy was used to image HepG2 cells after incubation with **DCMT** and **DCMC**; **DCMT-OH** and **DCMC-OH** were used as control. We determined that the fluorescence of both probes overlapped well with that of Mito tracker Green, a commercial mitochondrial tracker (Fig. 3A). A high Pearson correlation coefficient of 0.97 and 0.96 was observed for **DCMT** and **DCMC**, respectively (Fig. 3B). In contrast, **DCMT-OH** and **DCMC-OH** without the triphenyl-phosphonium group did not localize in the mitochondria of the cells (Fig. S24, ESI). In addition, the result of a subsequent photostability test showed that after 30 min of continuous irradiation, the fluorescence of **DCMT** and **DCMC** did not decrease sharply compared to the initial state, suggesting their good photostability in cells (Fig. S25, ESI).

PDT-induced cell death in vitro. Then, the PDT efficiency of **DCMT** and **DCMC** was evaluated. The intrinsic cytotoxicity of the probes for HepG2 cells was first evaluated in the dark. The cells were determined to be viable after incubation with the compounds (0-40 μM) for 24 hrs without light illumination (Fig. 4A). In contrast, when the cells pre-incubated with the probes were irradiated using broad-band light (22.7 mW cm^{-2}) for 100 min, concentration-dependent cell death was observed. The cell viability was reduced by 74% and 61% when cells were treated with 40 μM of **DCMT** (Fig. 4B) and **DCMC** (Fig. 4C), respectively. The enhanced PDT effect of **DCMT** over **DCMC** agrees with its higher $^1O_2$ conversion efficiency determined above. In contrast, **DCMT-OH** and **DCMC-OH** did not cause cell death irrespective of light irradiation (Fig. S26, ESI), which is consistent with the results obtained from solution-based tests. Additionally, the PDT efficiency of **DCMC/DCMT** was compared to that of the commercial photosensitizer, RB (Fig S27, ESI). With light irradiation (22.7 mW·cm^{-2}), the cell viability was reduced to 35%, 32% and 40% when the cells were treated with 20 μM of **DCMC**, **DCMT** and RB, respectively. This suggests a slightly better therapeutic efficacy of **DCMC** and **DCMT** than that of RB. However, the cell viability of **DCMT**- and RB-treated cells both decreased to 22% when the concentration of the agents reached 40 μM. This suggests that the PDT effect of the probes we synthesized saturated at a relatively lower concentration than the commercial reagent.

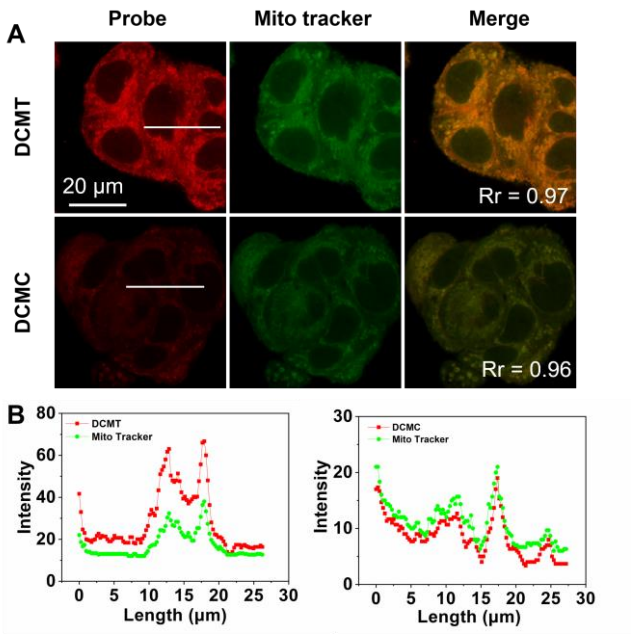

Figure 3. (A) Fluorescence co-localization of **DCMT** (5 μM) and **DCMC** (5 μM) with Mito Tracker (500 nM) in HepG2 cells. (B) Fluorescence quantification of **DCMT** (5 μM) and **DCMC** (5 μM) with Mito Tracker (500 nM) of a selected section of cells imaged.

To corroborate that the suppression of cell viability is the result of ROS generation in cells, a commercial ROS kit containing (2,7-dichloro-dihydro-fluorescein diacetate (DCFH-DA) was used.[51] DCFH-DA is oxidized by intracellular ROS to produce the fluorescent 2,7-dichloro-dihydro-fluorescein (DCF). As shown in Figure 5A and 5C, when HepG2 cells were treated with different concentrations of **DCMT** and **DCMC** under the irradiation of broad-band light (22.7 mW cm^{-2}), the green fluorescence emission of DCF increased as the concentration of **DCMT** and **DCMC** increased with light irradiation, suggesting the intracellular ROS levels increased in a concentration-dependent manner. **DCMT** was found to produce a ca. 5-fold increase in ROS levels at a concentration of 40 μM under light irradiation with respect to the group without light irradiation (Fig. 5B). In contrast, the ROS increased by ca. 1.5-fold for the **DCMC** group when light was used (Fig. 5D). This agrees with the result from MTS experiments where **DCMT** had a better PDT effect than **DCMC**. In addition, a live/dead cell staining assay was carried out (Fig. S28, ESI). As shown in Figure

S28A, when cells were treated with **DCMC** and **DCMT**, a strong fluorescence emission of EasyProbe Green 488 was observed under light irradiation, indicating a significant amount of cell death. In contrast, in the group without light irradiation, minimal fluorescence of EasyProbe Green 488 was seen. In addition, the dead cells produced were dependent on the concentration of the probes (Figure S28B).

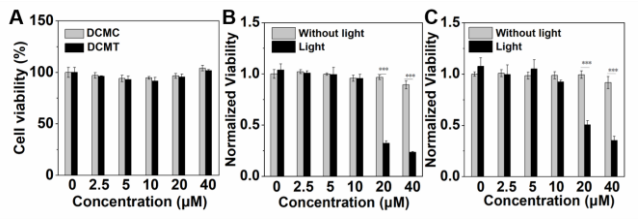

Figure 4. Cell viability of HepG2 after treatment with (A) various concentrations of **DCMT** and **DCMC** in the dark, (B) various concentrations of **DCMT** with and without white-light irradiation (22.7 mW cm^{-2}) for 100 min, and (C) various concentrations of **DCMC** with and without white-light irradiation (22.7 mW cm^{-2}) for 100 min, determined by the MTS assay. ***P < 0.001. Error bars represent S. D. (n = 3).

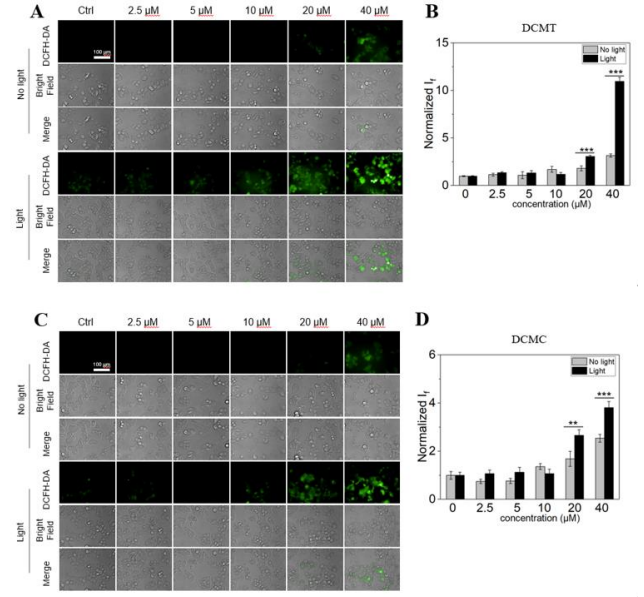

Figure 5. (A) Fluorescence images and (B) Fluorescence quantification of DCFH-DA (5 μM) in HepG2 cells after incubation with different concentrations of **DCMT** with or without white-light irradiation (22.7 mW·cm^{-2}); (C) Fluorescence images and (D) Fluorescence quantification of DCFH-DA (5 μM) in the HepG2 cells after incubation with different concentrations of **DCMC** with or without white-light irradiation (22.7 mW·cm^{-2}). **P < 0.01, ***P < 0.001. Error bars represent S. D. (n= 3).

CONCLUSIONS

To conclude, we have synthesized two mitochondria-targeting, AIE-active theranostic probes for the selective fluorescence imaging and PDT of liver cancer cells. The probes localized in the mitochondria of cells and resulted in cell death under light irradiation. The development of new theranostic systems based on other fluorescent dyes[52-59] is currently underway in our laboratories.

ASSOCIATED CONTENT

Supporting Information

The Supporting Information is available free of charge on the ACS Publications website at http://pubs.acs.org.

Figures showing NMR and HRMS characterization data for DCMT-OH/DCMC-OH and **DCMT/DCMC**, $^1O_2$ detection method and ROS-Generation detection of **DCMT/DCMC**, and additional data.

AUTHOR INFORMATION

Corresponding Author

*E-mail: cywang@ecust.edu.cn, (C. Wang)
*E-mail: xphe@ ecust.edu.cn (X.-P. He)
*E-mail: yzang@simm.ac.cn (Y. Zang)
*E-mail: t.d.james@bath.ac.uk (Tony D. James)

Author Contributions

‡D. Z. and H.-H. H contributed equally to this work.

Notes

The authors declare no competing financial interest.

ACKNOWLEDGMENT

The authors thank the National Natural Science Foundation of China (No. 21788102), the National Science and Technology Major Project of China (No. 2018ZX10732202), the Shanghai Municipal Science and Technology Major Project (No. 2018SHZDZX03), the International Cooperation Program of Shanghai Science and Technology Committee (No. 17520750100), and the Fundamental Research Funds for the Central Universities (222201717003) for financial support. TDJ wishes to thank the Royal Society for a Wolfson Research Merit Award and the Open Research Fund of the School of Chemistry and Chemical Engineering, Henan Normal University for support (2020ZD01). H.-H. H would like to thank the Project funded by China Postdoctoral Science Foundation (No. 2020M681196).

REFERENCES

(1) Hu, F.; Cai, X. L.; Manghnani, P. N.; Kenry; Wu, W. B.; Liu, B. Multicolor monitoring of cellular organelles by single wavelength excitation to visualize the mitophagy process. *Chem. Sci.* **2018**, 9, 2756-2761.

(2) Zhuang, W. H.; Yang, L.; Ma, B. X.; Kong, Q. S.; Li, G. C.; Wang, Y. B.; Tang, B. Z. Multifunctional two-photon AIE luminogens for highly mitochondria-specific bioimaging and efficient photodynamic therapy. *ACS Appl. Mater. Interfaces*. **2019**, 11, 20715-20724.

(3) Dai, J.; Wu, X.; Ding, S. Y.; Lou, X. D.; Xia, F.; Wang, S. X.; Hong, Y. N. Aggregation-induced emission photosensitizers: from molecular design to photodynamic therapy. *J. Med. Chem.* **2020**, 63, 1996-2012.

(4) Li, X. P.; Zhao, Y.; Zhang, T.; Xing, D. Mitochondria-specific agents for photodynamic cancer therapy: a key determinant to boost the efficacy. *Adv. Healthcare Mater.* **2021**, 10, 2001240.

(5) Celli, J. P.; Spring, B. Q.; Rizvi, I.; Evans, C. L.; Samkoe, K. S.; Verma, S.; Pogue, B. W.; Hasan, T. Imaging and

photodynamic therapy: mechanisms, monitoring, and optimization. *Chem. Rev.* **2010**, 110, 2795-2838.

(6) Cheng, L.; Wang, C.; Feng, L. Z.; Yang, K.; Liu, Z. Functional nanomaterials for phototherapies of cancer. *Chem. Rev.* **2014**, 114, 10869-10939.

(7) DeRosa, M. C.; Crutchley, R. J. Photosensitized singlet oxygen and its applications. *Coord. Chem. Rev.* **2002**, 233, 351-371.

(8) Juarranz, Á.; Jaén, P.; Sanz-Rodríguez, F.; Cuevas, J.; González, S. Photodynamic therapy of cancer. Basic principles and applications. *Clin. Transl. Oncol.* **2008**, 10, 148-154.

(9) Wu, X. M.; Sun, X. R.; Guo, Z. Q.; Tang, J. B.; Shen, Y. Q.; James, T. D.; Tian, H.; Zhu, W. H. In vivo and in situ tracking cancer chemotherapy by highly photostable NIR fluorescent theranostic prodrug. *J. Am. Chem. Soc.* **2014**, 136, 3579-3588.

(10) Kim, E. J.; Bhuniya, S.; Lee, H.; Kim, H. M.; Cheong, C.; Maiti, S.; Hong, K. S.; Kim, J. S. An activatable prodrug for the treatment of metastatic tumors. *J. Am. Chem. Soc.* **2014**, 136, 13888-13894.

(11) Kumar, R.; Han, J.; Lim, H. J.; Ren, W. X.; Lim, J. Y.; Kim, J. H.; Kim, J. S. Mitochondrial induced and self-monitored intrinsic apoptosis by antitumor theranostic prodrug: in vivo imaging and precise cancer treatment. *J. Am. Chem. Soc.*, **2014**, 136, 17836-17843.

(12) Lee, M. H.; Kim, J. Y.; Han, J. H.; Bhuniya, S.; Sessler, J. L.; Kang, C.; Kim. J. S. Direct fluorescence monitoring of the delivery and cellular uptake of a cancer-targeted RGD peptide-appended naphthalimide theragnostic prodrug. *J. Am. Chem. Soc.* **2012**, 134, 12668-12674.

(13) Liu, Y. J.; Zhu, S. J.; Gu, K. Z.; Guo, Z. Q.; Huang, X. Y.; Wang, M. W.; Amin, H. M.; Zhu, W. H.; Shi, P. GSH-activated NIR fluorescent prodrug for podophyllotoxin delivery. *ACS Appl. Mater. Interfaces*. **2017**, 9, 29496-29504.

(14) Xiao, M.; Sun, W.; Fan, J. L.; Cao, J. F.; Li, Y. Q.; Shao, K.; Li, M.; Li, X. J.; Kang, Y.; Zhang, W. D.; Long, S.; Du, J. J.; Peng, X. J. Aminopeptidase-N-activated theranostic prodrug for NIR tracking of local tumor chemotherapy. *Adv. Funct. Mater*. **2018**, 28, 1805128.

(15) Zheng, Y. Q.; Yu, B. C.; Li, Z.; Yuan, Z. N.; Organ, C. L.; Trivedi, R. K.; Wang, S.; Lefer, D. J.; Wang, B. H. An esterase-sensitive prodrug approach for controllable delivery of persulfide species. *Angew. Chem. Int. Ed.* **2017**, 56,11749-11753.

(16) Gu, Z. K.; Dong, Y.; Xu, S. X.; Wang L. S.; Liu, Z. Molecularly imprinted polymer-based smart prodrug delivery system for specific targeting, prolonged retention, and tumor microenvironment-triggered release. *Angew. Chem. Int. Ed.* **2021**, 60, 2663-2667.

(17) Popova, M.; Soboleva, T.; Ayad, S.; Benninghoff, A. D.; Berreau, L. M. Visible-light-activated quinolone carbon-monoxide-releasing molecule: prodrug and albumin-assisted delivery enables anticancer and potent anti-inflammatory effects. *J. Am. Chem. Soc.* **2018**, 140, 9721-9729.

(18) Chen, J. Y.; Zhang, Y. D.; Meng, Z.; Guo, L.; Yuan, X. Y.; Zhang, Y. H.; Chai, Y.; Sessler, J. L.; Meng, Q. B.; Li, C. J. Supramolecular combination chemotherapy: a pH-responsive co-encapsulation drug delivery system. *Chem. Sci.* **2020**, 11, 6275-6282.

(19) Gao, M.; Yu, F. B.; Lv, C. J.; Choo, J.; Chen, L. X. Fluorescent chemical probes for accurate tumor diagnosis and targeting therapy. *Chem. Soc. Rev.* **2017**, 46, 2237-2271.

(20) Leea, M. H.; Sharma, A.; Chang, M. J.; Lee, J.; Son, S.; Sessler, J. L.; Kang C.; Kim, J. S. Fluorogenic reaction-based prodrug conjugates as targeted cancer theranostics. *Chem. Soc. Rev.* **2018**, 47, 28-52.

(21) Sharma, A.; Arambula, J. F.; Koo, S.; Kumar, R.; Singh, H.; Sessler, J. L.; Kim, J. S. Hypoxia-targeted drug delivery. *Chem. Soc. Rev.* **2019**, 48, 771-813.

(22) Ji X. Y.; Wang, B. H. *Acc.* Strategies toward organic carbon monoxide prodrugs. *Chem. Res.* **2018**, 51, 1377-1385.

(23) Maiti, S.; Park, N.; Han, J. H.; Jeon, H. M.; Lee, J. H.; Bhuniya, S.; Kang, C.; Kim, J. S. Gemcitabine-coumarin-biotin conjugates: a target specific theranostic anticancer prodrug. *J. Am. Chem. Soc.* **2013**, 135, 4567-4572.

(24) Li, S. Y.; Liu, L. H.; Jia, H. Z.; Qiu, W. X.; Rong, L.; Cheng, H.; Zhang, X. Z. A pH-responsive prodrug for real-time drug release monitoring and targeted cancer therapy. *Chem. Commun.* **2014**, 50, 11852-11855.

(25) Luo, J. D.; Xie, Z. L.; Lam, J. W. Y.; Cheng, L.; Chen, H. Y.; Qiu, C. F.; Kwok, H. S.; Zhan, X. W.; Liu, Y. Q.; Zhu, D. B.; Tang, B. Z. Aggregation-induced emission of 1-methyl-1,2,3,4,5-pentaphenylsilole. *Chem. Commun.* **2001**, 21, 1740-1741.

(26) Hong, Y. N. Aggregation-induced emission-fluorophores and applications. *Methods Appl. Fluoresc.* **2016**, 4, 022003.

(27) Mei, J.; Leung, N. L. C.; Kwok, R. T. K.; Lam J. W. Y.; Tang, B. Z. Aggregation-induced emission: together we shine, united we soar. *Chem. Rev.*, **2015**, 115, 11718-11940.

(28) Hu, F.; Xu, S. D.; Liu, B. Photosensitizers with aggregation-induced emission: materials and biomedical applications. *Adv. Mater.* **2018**, 30, 1801350.

(29) Dou, W.T.; Qin, Z.Y.; Li, J.; Zhou D.M.; He, X.P. Self-assembled sialyllactosyl probes with aggregation-enhanced properties for ratiometric detection and blocking of influenza viruses. *Sci. Bull.* **2019**, 64, 1902.

(30) Wan, Q.; Zhang, R. Y.; Zhuang, Z. Y.; Li, Y. X.; Huang, Y. H.; Wang, Z. M.; Zhang, W. J.; Hou, J. Q.; Tang. B. Z. Molecular engineering to boost AIE-active free radical photogenerators and enable high-performance photodynamic therapy under hypoxia. *Adv. Funct. Mater.* **2020**, 30, 2002057.

(31) Zhao, W. J.; He, Z. K.; Tang, B. Z. Room-temperature phosphorescence from organic aggregates. *Nat. Rev. Mater.* **2020**, 5, 869-885.

(32) Qian, M.; Zhang, L. W.; Wang, J. Y.; Peng, X. J. A red-emitting fluorescent probe with large stokes shift for real-time tracking of cysteine over glutathione and homocysteine in living cells. *Spectrochem. ACTA A.* **2019**, *214*, 469-475.

(33) Huang, H.; Tian, Y. A ratiometric fluorescent probe for bioimaging and biosensing of HBrO in mitochondria upon oxidative stress. *Chem. Commun.* **2018**, 54, 12198-12201.

(34) Zhang, W. J.; Huo, F. J.; Yin, C. X. Recent advances of dicyano-based materials in biology and medicine. *J. Mater. Chem. B.* **2018**, 6, 6919-6929.

(35) Zielonka, J.; Joseph, J.; Sikora, A.; Hardy, M.; Ouari, O.; Vasquez-Vivar, J.; Cheng, G.; Lopez, M.; Kalyanaraman, B. Mitochondria-targeted triphenylphosphonium-based compounds: syntheses, mechanisms of action, and therapeutic

and diagnostic applications. *Chem. Rev.* **2017**, 117, 10043-10120.

(36) Li, N.; Yu, L. H.; Wang, J. B.; Gao, X. N.; Chen, Y. Y.; Pan, W.; Tang, B. A mitochondria-targeted nanoradiosensitizer activating reactive oxygen species burst for enhanced radiation therapy. *Chem. Sci.* **2018**, 9, 3159-3164.

(37) Wu, W. B.; Mao, D.; Xu, S. D.; Ji, S. L.; Hu, F.; Ding, D.; Kong, D. L.; Liu, B. High performance photosensitizers with aggregation-induced emission for image-guided photodynamic anticancer therapy. *Mater. Horiz.* **2017**, 4, 1110-1114.

(38) M. X. Liu, L. L. Ma, X. Y. Liu, J. Y. Liu, Z. L. Lu, R. Liu and L. He, Combination of [12]aneN_3 and triphenylamine-benzylideneimidazolone as nonviral gene vectors with two-photon and AIE properties. *ACS Appl. Mater. Interfaces*. **2019**, 11, 42975-42987.

(39) Wang, D. H.; Chen, L. J.; Zhao, X.; Yan, X. P. Enhancing near-infrared AIE of photosensitizer with twisted intramolecular charge transfer characteristics via rotor effect for AIE imaging-guided photodynamic ablation of cancer cells. *Talanta*. **2021**, 225, 122046.

(40) Deng, K. L.; Wang, L.; Xia, Q.; Liu, R. Y.; Qu, J. Q. A turn-on fluorescent chemosensor based on aggregation-induced emission for cyanide detection and its bioimaging applications. *Sens. Actuator B-Chem.* **2019**, 296, 126645.

(41) Hong, Y. N.; Lam, J. W. Y.; Tang, B. Z. Aggregation-induced emission: phenomenon, mechanism and applications. *Chem. Commun.* **2009**, 29, 4332-4353.

(42) Jiang, M. J.; Kwok, R. T. K.; Li, X. S.; Gui, C.; Lam, J. W. Y.; Qu, J. N.; Tang, B. Z. A simple mitochondrial targeting AIEgen for image-guided two-photon excited photodynamic therapy. *J. Mater. Chem. B.* **2018**, 6, 2557-2565.

(43) Li, Y. B.; Zhu, Y. L.; Cai, X. Z.; Guo, J. M.; Yao, C. P.; Pan, Q. L.; Wang, X. F.; Wang, K. N. A benzothiazole-based near-infrared fluorescent probe for sensing SO_2 derivatives and viscosity in HeLa cells. *Spectroc. Acta Pt. A-Molec. Biomolec. Spectr.* **2021**, 251, 119457.

(44) Zhou, K.; Ren, M. G.; Deng, B. B.; Lin, W.Y. Development of a viscosity sensitive fluorescent probe for real-time monitoring of mitochondria viscosity. *New J. Chem.* **2017**, 41, 11507-11511.

(45) Zhang, X.; Gan, X. P.; Yao, S.; Zhu, W. J.; Yu, J. H.; Wu, Z. C.; Zhou, H. P.; Tian, Y. P.; Wu, J. Y. Branched triphenylamine-core compounds: aggregation induced two-photon absorption. *RSC Adv.* **2016**, 6, 60022-60028.

(46) Xu, J. Z.; Zhang, H. J.; Xu, Z.; Tao, F. R.; Cui, Y. Z.; Yu, W. W. Chemosensing test paper based on aggregated nanoparticles of a barbituric acid derivative. *J. Nanomater.* **2020**, 2020, 7826231.

(47) Zhuang, W. H.; Yang, L.; Ma, B. X.; Kong, Q. S.; Li, G. C.; Wang, Y. B.; Tang, B. Z. Multifunctional two-photon AIE luminogens for highly mitochondria-specific bioimaging and efficient photodynamic therapy. *ACS Appl. Mater. Interfaces.* **2019**, 11, 20715-20724.

(48) Wang, S. W.; Chen, H.; Liu, J.; Chen, C. J.; Liu, B. NIR-II light activated photosensitizer with aggregation-induced emission for precise and efficient two-photon photodynamic cancer cell ablation. *Adv. Funct. Mater*. **2020**, 30, 2002546.

(49) Kong, Q. S.; Ma, B. X.; Yu, T.; Hu, C.; Li, G.C.; Jiang, Q.; Wang, Y. B. A two-photon AIE fluorophore as a photosensitizer for highly efficient mitochondria-targeted photodynamic therapy. *New J. Chem*. **2020**, 44, 9355.

(50) Liu, Z. Y.; Zou, H.; Zhao, Z.; Zhang, P. F.; Shan, G. G.; Kwok, R. T. K.; Lam, J. W. Y.; Zheng, L.; Tang, B. Z. Tuning organelle specificity and photodynamic therapy efficiency by molecular function design. *ACS Nano*. **2019**, 13, 11283-11293.

(51) Zou, J. L.; Zhang, Y.; Sun, J. B.; Wang, X. Y.; Tu, H. L.; Geng, S.; Liu, R. H.; Chen, Y. X.; Bi, Z. G. Deoxyelephantopin induces reactive oxygen species-mediated apoptosis and autophagy in human osteosarcoma cells. *Cell. Physiol. Biochem.* **2017**, 42, 1812-1821.

(52) He, X. P.; Zeng, Y.L.; Tang, X.Y.; Li, N.; Zhou, D.M.; Chen, G.R.; Tian, H. Rapid identification of the receptor-binding specificity of influenza a viruses by fluorogenic glycofoldamers. *Angew. Chem. Int. Ed.* **2016**, 55, 13995.

(53) Zhang, J.; Fu, Y.; Han, H.H.; Zang, Y.; Li, J.; He, X.P.; Feringa, B. L.; Tian, H. Remote light-controlled intracellular target recognition by photochromic fluorescent glycoprobes. *Nat. Commun.* **2017**, 8, 987.

(54) Sedgwick, A. C.; Dou, W.T.; Jiao, J.B.; Wu, L.; Williams, G. T.; Jenkins, A. T. A.; Bull, S. D.; Sessler, J. L.; He X.P.; James, T. D. An ESIPT probe for the ratiometric imaging of peroxynitrite facilitated by binding to Aβ-aggregates. *J. Am. Chem. Soc.* **2018**, 140, 14267.

(55) Fu, Y.; Han, H.H.; Zhang, J.; He, X.P.; Feringa, B. L.; Tian, H. Photocontrolled fluorescence "double-check" bioimaging enabled by a glycoprobe-protein hybrid. *J. Am. Chem. Soc.* **2018**, 140, 8671.

(56) Hu, X.L.; Kwon, N.; Yan, K.C.; Sedgwick, A. C.; Chen, G.R.; He, X.P.; James, T. D.; Yoon, J. Bio-conjugated advanced materials for targeted disease theranostics. *Adv. Funct. Mater.* **2020**, 30, 1907906.

(57) Chai, X.; Han, H.H.; Sedgwick, A. C.; Li, N.; Zang, Y.; James, T. D.; Zhang, J.; Hu, X.L.; Yu, Y.; Li, Y.; Wang, Y.; Li, J.; He, X.P.; Tian, H. Photochromic fluorescent probe strategy for the super-resolution imaging of biologically important biomarkers. *J. Am. Chem. Soc.* **2020**, 142, 18005.

(58) Jiao, J.B.; Wang, G.Z.; Hu, X.L.; Zang, Y.; Maisonneuve, S.; Sedgwick, A. C.; Sessler, J. L.; Xie, J.; Li, J.; He, X.P.; Tian, H. Cyclodextrin-based peptide self-assemblies (Spds) that enhance peptide-based fluorescence imaging and antimicrobial efficacy. *J. Am. Chem. Soc.* **2020**, 142, 1925.

(59) Han, H.-H.; Tian, H.; Zang, Y.; Sedgwick, A. C.; Li, J.; Sessler, J. L.; He, X.-P.; James, T. D., Small-molecule fluorescence-based probes for interrogating major organ diseases. *Chem. Soc. Rev.* **2021**. https://doi.org/10.1039/D0CS01183E.

for TOC only

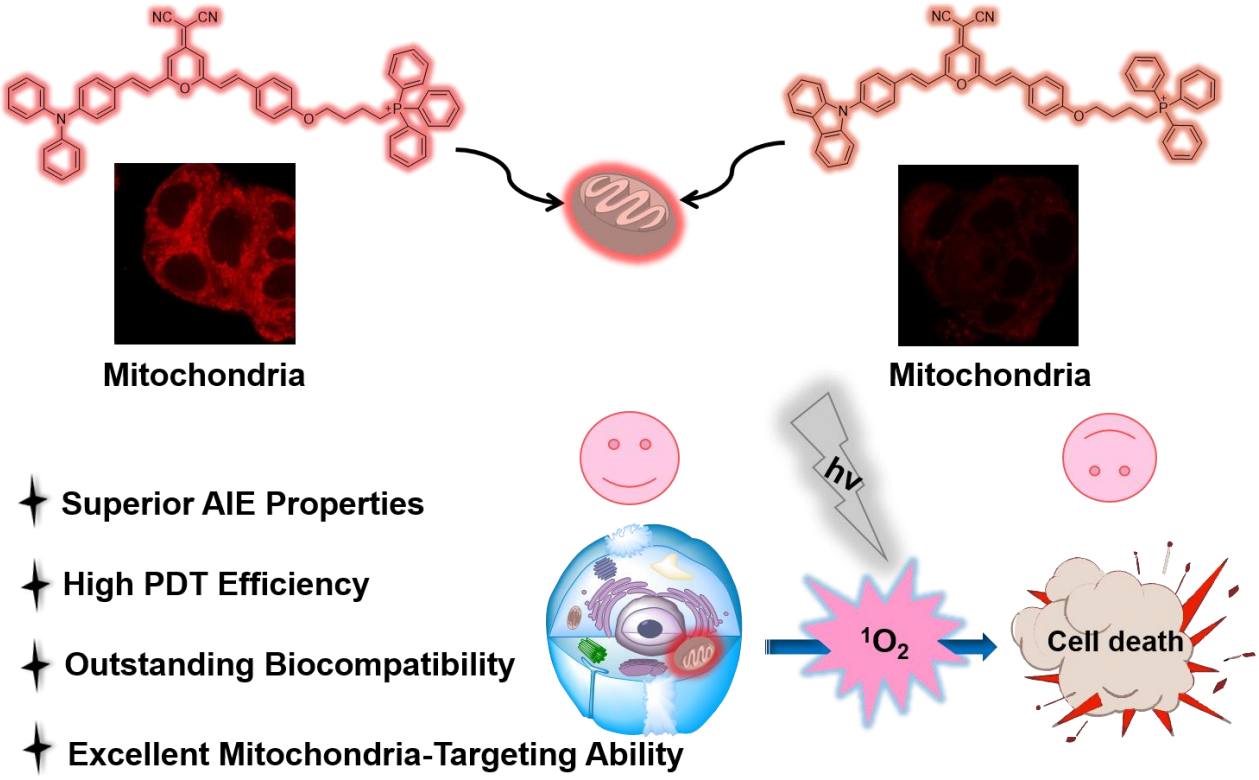
Mitochondria
Mitochondria
Superior AIE Properties
High PDT Efficiency
Outstanding Biocompatibility
Excellent Mitochondria-Targeting Ability
hv
$^1O_2$
Cell death